Cell Reports
Physical Science

CellPress
OPEN ACCESS

Article

The influence of dissolved gas supersaturation on bubble detachment from planar (photo) electrodes

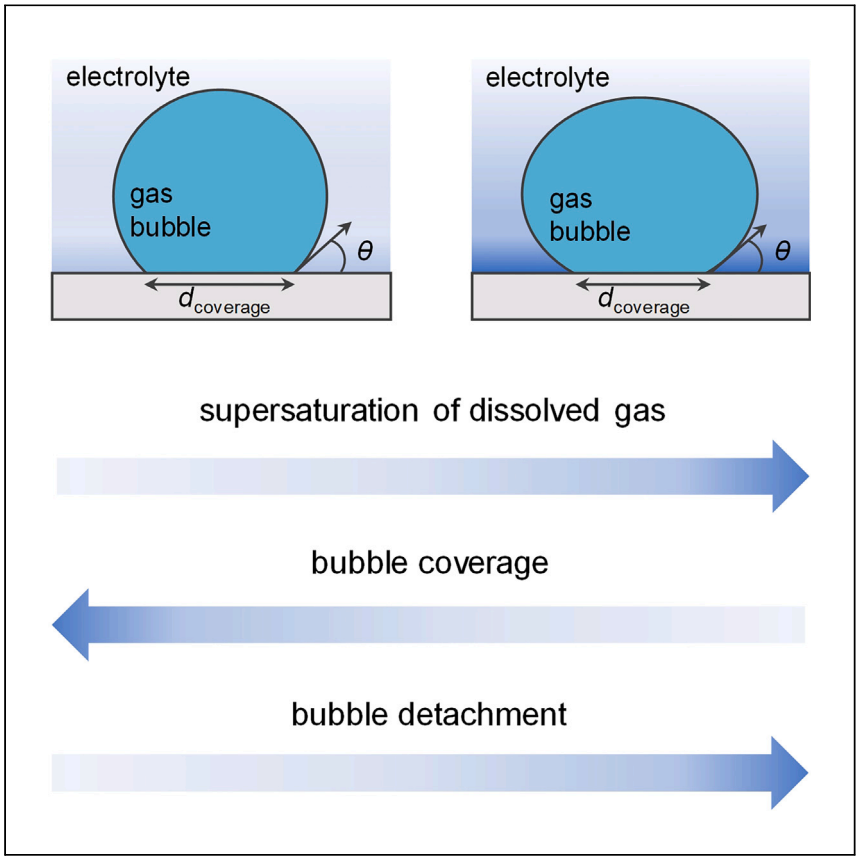

The presence of bubbles on the surface of (photo)electrodes introduces various loss factors. Liang et al. introduce multiphysics simulations based on the level-set method, highlighting the important parameters that facilitate oxygen bubble detachment from the surface of (photo)electrodes to minimize bubble-induced losses.

Feng Liang, Roel van de Krol, Fatwa F. Abdi

ffabdi@cityu.edu.hk

Highlights

Multiphysics level-set model simulates bubble detachment from (photo)electrode

Supersaturated boundary layer of dissolved gas facilitates bubble detachment

Surface tension forces dominate bubble detachment behavior

Practical solutions to minimize bubble-induced losses are discussed

Liang et al., Cell Reports Physical Science 5, 102069
July 17, 2024 © 2024 The Authors. Published by Elsevier Inc.
https://doi.org/10.1016/j.xcrp.2024.102069

Cell Reports
Physical Science

CellPress
OPEN ACCESS

Article

The influence of dissolved gas supersaturation on bubble detachment from planar (photo)electrodes

Feng Liang,[1] Roel van de Krol,[1,2] and Fatwa F. Abdi[1,3,4,*]

SUMMARY

In this study, we explore the detachment process of oxygen bubbles from a (photo)electrode, with a focus on the often-overlooked influence of a supersaturated boundary layer of dissolved oxygen near the (photo)electrode surface. Numerical simulations were performed to examine subtle changes of the shape of the bubbles at the bubble-electrolyte interface. The presence of the supersaturated boundary layer is found to distort the interface and facilitate bubble detachment by reducing the surface tension force. Parametric investigation of various factors, such as supersaturation levels, boundary layer thickness, electrolyte flow rate, and contact angle were performed to understand how they affect bubble detachment. Surface tension forces are found to dominate bubble detachment behavior over buoyancy, and the solutal Marangoni effect induced shear forces. Based on these findings, several practical engineering considerations for minimizing bubble-induced losses in (photo)electrochemical devices are discussed.

INTRODUCTION

Many (photo)electrochemical devices involve the generation of bubbles, such as hydrogen and oxygen, the presence of which has various consequences. For example, bubbles may block the active area of the (photo)electrocatalyst surface,[1] resulting in a decrease in performance. They may also obstruct the ion-conducting pathways in the electrolyte and increase the overpotential. Moreover, under certain operating conditions, the presence of bubbles can promote product crossover.[2] Indeed, removing bubbles in a water electrolysis cell by, for example, ultrasonic agitation, has been reported to increase the current density by 15%–18% and decrease the overpotential by up to 25%.[3,4] The detrimental effects of bubbles have also been demonstrated in all-vanadium redox flow cell batteries, where undesired oxygen and hydrogen bubble evolution negatively impact the cell performance due to partial obstruction of electrolyte flow, decrease in the active surface area, and reduced mass and charge transfer coefficients of the redox species.[5,6] In photoelectrochemical devices, where light often needs to penetrate through the electrolyte to reach the photoelectrode, bubbles also induce optical losses due to reflection and scattering.[7] Many strategies have been proposed and tested to minimize bubble-induced losses, such as forced electrolyte flow,[1,8,9] electrode surface engineering,[10,11] addition of surfactants,[12,13] or application of magnetic or acoustic fields.[14–17] While they can be somewhat effective, the role of these engineering measures in controlling bubble dynamics is not yet fully understood.

[1]Institute for Solar Fuels, Helmholtz-Zentrum Berlin für Materialien und Energie GmbH, 14109 Berlin, Germany

[2]Technische Universität Berlin, Department of Chemistry, 10623 Berlin, Germany

[3]School of Energy and Environment, City University of Hong Kong, Kowloon, Hong Kong, SAR, China

[4]Lead contact

*Correspondence: ffabdi@cityu.edu.hk

https://doi.org/10.1016/j.xcrp.2024.102069

This is an open access article under the CC BY license (http://creativecommons.org/licenses/by/4.0/).

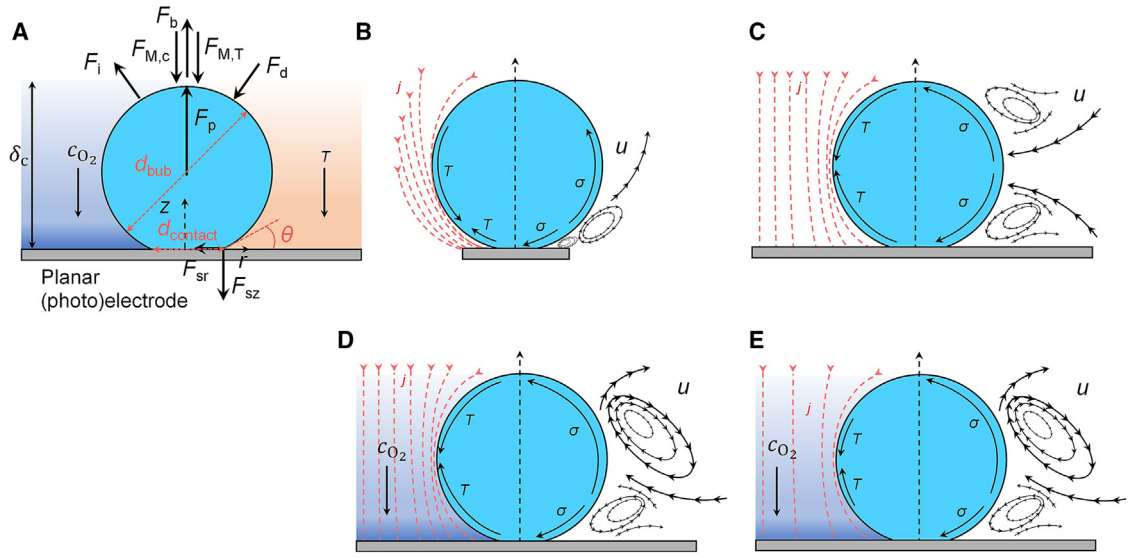

Figure 1. Schematic illustration of a bubble adhering on a (photo)electrode surface

(A) Forces acting on an oxygen bubble adhering on a planar (photo)electrode. d_{bub} is the bubble diameter, $d_{contact}$ is the diameter of the bubble contact region on the (photo)electrode, θ represents the bubble contact angle, c_{O_2} is the concentration of the dissolved oxygen, δ_c is the thickness of the SSBL, and T is the temperature. Various forces act on this bubble, and its balance determines the detachment. F_M is the Marangoni force, which develops due to, for example, the concentration gradient ($F_{M,c}$) and the temperature gradient ($F_{M,T}$). F_i is the inertia force, F_d is the hydrodynamic drag force, F_b is the buoyancy force, F_p is the pressure force, F_{sz} is the surface tension force in the z direction, and F_{sr} is the surface tension force in the radial (r) direction.

(B–D) Schematic illustration of a bubble adhering to a microelectrode (prior to detachment), indicating that the current density (j) distribution induces gradients of temperature and the surface tension coefficient (σ). The same processes on a relatively large planar electrode, (C) in the absence or (D) in the presence of the SSBL of dissolved oxygen are also illustrated.

(E) Schematic illustration of a bubble adhering to a planar (photo)electrode (prior to detachment), in the presence of the SSBL of oxygen, with relatively low current density. The velocity of the Marangoni convection is indicated by u.

There are several stages of bubble formation in (photo)electrochemical devices. Reaction products generated from the (photo)electrode surface first diffuse into the electrolyte as dissolved gas and form a supersaturated region at the vicinity of the electrodes. Bubbles start to form on (or near[11]) the electrodes once the concentration exceeds the solubility limit of the electrolyte.[18,19] After nucleation, bubble growth is governed by several mechanisms across various timescales. During the first few tens of microseconds, bubbles grow linearly, and the growth is controlled by inertia.[20] Later on, diffusion-controlled bubble growth takes place—in other words, gas molecules diffuse into bubbles from the supersaturated region of the liquid electrolyte.[21] Throughout this bubble growth period, a portion of the electrode surface is deactivated as contact with the electrolyte is prevented. Bubble detachment occurs when the bubble diameter exceeds a critical value, thereby freeing the electrode surface for further electrochemical reactions as contact with fresh electrolyte is re-established. These processes are repeated and often result in a periodic bubble formation pattern.

One general approach to minimize bubble-induced losses is by ensuring that bubbles detach easily from the electrode surface. The mechanism behind bubble detachment is, however, not trivial. Figure 1A is a schematic drawing of various forces acting on a growing oxygen bubble. The bubble detaches from a gas-evolving electrode when the upward force components in the z direction (e.g., buoyancy force, F_b, and pressure force, F_p) cancel out those in the opposite direction (e.g., surface tension force, F_{sz}, and Marangoni force, F_M). Several force balance models that consider or ignore some of these forces have been proposed to

determine the critical bubble detachment diameter. For example, Fritz's equation, in which bubble departure is governed by the F_b and surface tension, has been applied successfully in several scenarios—for example, pool nucleate boiling[22] and electrolytic bubble formation.[9,23–25] However, this equation is insufficient to explain specific phenomena during bubble departure, such as bubble oscillation on microelectrodes.[26] Such mismatches are usually overcome by including a more thorough force analysis during bubble detachment. For example, the Marangoni effect (indicated as F_M in Figure 1A) was pointed out by Lubetkin[27] and has recently drawn much attention,[24,26,28–30] although its exact contribution to bubble detachment remains ambiguous. In principle, the Marangoni effect is governed by the gradient of surface tension coefficient (σ) at the gas-electrolyte interface, which depends on the temperature (T), the electric potential (V), the electrolyte composition,[31] and the concentration of the dissolved species (c).[26,30] Note that the ion concentration gradient in the electrolyte can also induce a solutal Marangoni effect, which is well reported by Park et al.,[31] and it should differ from the Marangoni effect in our study. The relative size of the gas-evolving electrode (compared to the bubble size) also affects the resulting Marangoni effect. Many researchers performed bubble generation-detachment experiments using a microelectrode (e.g., platinum wire encapsulated in a glass tube), as illustrated in Figure 1B. In such a configuration, the concentration-dependent Marangoni effect due to dissolved gases is often overlooked due to the following reasons. Currents are concentrated at the foot of the bubble, resulting in a localized Joule heating of the wedge-like volume of the electrolyte. Indeed, a temperature difference of more than 20 K has been observed near the foot of the bubble.[32] Moreover, less than 10% of the gas produced by these microelectrodes actually dissolves in the electrolyte.[31] Therefore, the temperature-dependent Marangoni effect dominates in these microelectrode experiments. When a large (planar) electrode is considered, which is more likely in practical applications, localized Joule heating moves upward to the bubble equator (see Figure 1C). This results in a more symmetrical and less dominant temperature-induced Marangoni effect. At the same time, it has been suggested that ~50% of all the gas produced (at room temperature and 1 atm) dissolves in the electrolyte.[33] The concentration-dependent Marangoni effect due to dissolved gases therefore becomes considerable, and the Marangoni convection pattern will change as this effect is included (see Figure 1D).

In this work, we focus on bubble detachment from a planar (photo)electrode, as illustrated in Figure 1E. We focus on conditions that are representative for photoelectrochemical processes under irradiation with non-concentrated sunlight. The operating current density for such processes is typically less than 20 mA cm^{-2}, which is much lower than in typical electrolyzers for hydrogen production (0.5–2 A cm^{-2}). It is therefore expected that the potential-dependent and the temperature-dependent Marangoni effects are negligible compared to the concentration-dependent Marangoni effect. This is especially true when a supersaturated boundary layer (SSBL) of the dissolved gas is formed near the planar electrode. Moreover, interactions between the neighboring bubbles and their effect on bubble detachment can be neglected due to dispersed bubble formation under this relatively low current density. We use multiphysics modeling based on the level-set method to investigate the impact of the SSBL on the detachment of an oxygen bubble from a planar (photo)anode. The surface tension between the gaseous oxygen and the liquid electrolyte is considered, and the electrolyte viscosity depends on the concentration of dissolved oxygen in the electrolyte. We consider various parameters, such as the level of oxygen supersaturation, the thickness of the SSBL, and the oxygen bubble contact angle, and report their impact on bubble detachment. Those parameters were chosen based

on two reasons. First, as schematically illustrated in Figure 1, the level of oxygen supersaturation, the thickness of the SSBL, and the oxygen bubble contact angle are the dominant factors in affecting bubble detachment from a planar (photo)electrode. Second, in practice, these parameters can be tuned to facilitate bubble detachment via cell/electrode engineering (e.g., changing the operating pressure, electrolyte flow rate, wettability of the (photo)electrodes). Our findings unravel important correlations between, for example, forced convection and bubble departure from the surface of the electrode. Several practical implications for device design and electrolyte engineering are discussed, and the potential benefits of operating (photo)electrochemical devices at elevated pressure are outlined.

RESULTS AND DISCUSSION

Impact of SSBL properties on O_2 bubble detachment

A schematic representation of our model and the accompanying boundary conditions are shown in Figure S1. Further details, including model validation, are described in the experimental procedures. In short, axisymmetric, two-dimensional (2D) multiphysics simulations are performed for an oxygen bubble generated from a horizontal electrode. We consider that the system is at the following state: an SSBL of dissolved oxygen has completely developed within the vicinity of the electrode. Due to limited solubility of oxygen in the electrolyte, bubble generation happens periodically at a nucleation site, followed by growth and detachment from the electrode. Since bubble detachment introduces a major disruption on the (photo)electrode surface, our simulations focus on the short period (5 ms) when the bubble departs the surface and how it is affected by the preexisting SSBL of dissolved oxygen. Other stages of bubble evolution (e.g., bubble nucleation, bubble growth) are therefore not included in the simulation. Within our short period of simulation time, diffusion of dissolved oxygen is unlikely to play a role. Indeed, the Péclet numbers (*Pe*) in our simulations are about 10^4 (i.e., $\gg 1$), indicating that diffusive mass transfer is negligible compared to convective mass transfer. Note that the interfacial mass transfer of the dissolved oxygen is not included in our model. The motion of the bubble-electrolyte interface is simulated with the level-set model. A level-set function (ϕ) of 0.5 is considered at the bubble-electrolyte interface. Unless otherwise mentioned, the size of the bubble (d_{bub}) is 1 mm, which is defined as the equivalent bubble diameter. This size is chosen for two reasons. First, previous experimental studies showed that oxygen bubbles of this size are able to detach from the electrode.[24] Second, our simulation revealed that parasitic current, a known numerical artifact in the level-set model,[34] is negligible for a bubble of this size (i.e., $d_{bub} > 0.5$ mm). Another limitation of this method is that the accuracy is largely sensitive to the mesh resolution, especially near the interface.[35] We overcome this limitation by starting every simulation case with the same 90° contact angle to ensure no additional artifacts due to different geometry and mesh settings. The contact angle was assigned to the pre-defined value automatically after the first time step. This is possible since the bubble-electrode interface is defined as the wetted wall boundary condition in our model, which is based on the Navier slip law (see Figure S1B). Note that the contact angle in our simulations is considered to be the apparent contact angle, which is the angle between the tangent to the liquid-gas interface and the line representing the nominal solid surface.[36] Changes in the contact angle are considered to be a result of the hydrophilicity (or wettability) variation of the (photo)electrode in our model.

We first discuss the impact of dissolved oxygen concentration on bubble detachment. The dissolved oxygen concentration (c_{O_2}) varies from 0 mM (i.e., no dissolved

oxygen in the electrolyte) to 300 mM in our simulations. The boundary layer thickness and the bubble contact angle are kept at 1 mm and 60°, respectively. The upper limit of c_{O_2} (300 mM) is chosen based on SuperHenry's law.[37] Although the maximum concentration of dissolved oxygen (prior to bubble nucleation) in water at room temperature and atmospheric pressure can only reach a supersaturated level of 120 mM (~100 times of the equilibrium solubility), higher operating pressure and temperature (e.g., up to 100 atm and 80°C) can result in supersaturated dissolved oxygen concentrations of 300 mM. Note that homogeneous bubble nucleation is assumed. Furthermore, according to an evaluation from Lubetkin,[27] the supersaturation of dissolved O_2 during water electrolysis can increase the Marangoni force by $-\partial\sigma/\partial c_{O_2} = 0.078\ \mathrm{N\,m^2}$. For comparison, we obtain $-\partial\sigma/\partial c_{O_2} = 0.074\ \mathrm{N\,m^2}$, which is very close to the reported value, by assuming ∂c_{O_2} between the vicinity of the electrode and the bulk as 300 mM and replacing the values with those in Figure S2E. Figures 2A–2E show the simulation results for various dissolved oxygen concentrations at t = 0–5 ms. When the dissolved oxygen concentration is large, the oxygen bubble departs the surface earlier, as shown by the color maps in Figures 2A and 2B (c_{O_2} = 300 and 200 mM) vs. those in Figures 2C and 2D (c_{O_2} = 100 and 50 mM). This observation is also shown in Figure 2F, where the bubble coverage of the electrode is plotted as a function of time. Notice that bubble detachment, identified as zero bubble coverage, occurs earlier with increasing c_{O_2}. When there is no dissolved oxygen in the electrolyte (i.e., c_{O_2} = 0 mM), the bubble fails to detach from the electrode (see Figures 2E and 2F). For better visualization, Videos S1 and S2, which cover the whole simulation time for the case with and without SSBL, respectively, have also been provided. These results suggest that the existence of the SSBL of dissolved oxygen facilitates bubble departure from the (photo) electrode.

The observation above is initially surprising in view of recent reports that show that Marangoni convection induced by concentration gradients imposes shear stress on the bubble-electrolyte interface.[26,27,30,38] The integration of this shear stress over the entire bubble-electrolyte interface results in a stress vector toward the electrode (i.e., opposing the bubble departure trajectory). Since other contributions to Marangoni effects can be ignored in our case, the Marangoni force can be written as

$$F_M = F_{M,c} = \oint_{l_{int}} c_{O_2} \cdot \frac{d\sigma}{dc_{O_2}}\, dl \qquad \text{(Equation 1)}$$

where $F_{M,c}$ is the Marangoni force component induced by the concentration gradient, l_{int} is the length of the bubble-electrolyte interface, and σ is the surface tension coefficient. A closer look at the simulation results provides an explanation for our observation. Although the average Marangoni force hinders bubble departure, and the direction does not change with varying c_{O_2} (see Figure 2H), the force distribution throughout the bubble-electrolyte interface varies with different c_{O_2} in the SSBL. An example of the $d\sigma/dc_{O_2}$ distribution along the bubble-electrolyte interface and the corresponding velocity are shown in Figure S3. This in turn results in a noticeable change in the morphology of the bubble at the bubble-electrolyte interface (see, e.g., bubble shape at t = 1 ms in Figures 2A–2E). Specifically, as also shown in Figure 2F, the diameter of the bubble contact with the electrode ($d_{contact}$) becomes smaller. As a result, the F_{sz} decreases according to the following equation:[24,39]

$$F_{sz} = \pi d_{contact} \sigma \sin\theta \qquad \text{(Equation 2)}$$

Here, θ is the contact angle. Indeed, these expected trends for F_M and F_{sz} are observed from our simulation results (see Figures 2G and 2H). These two forces

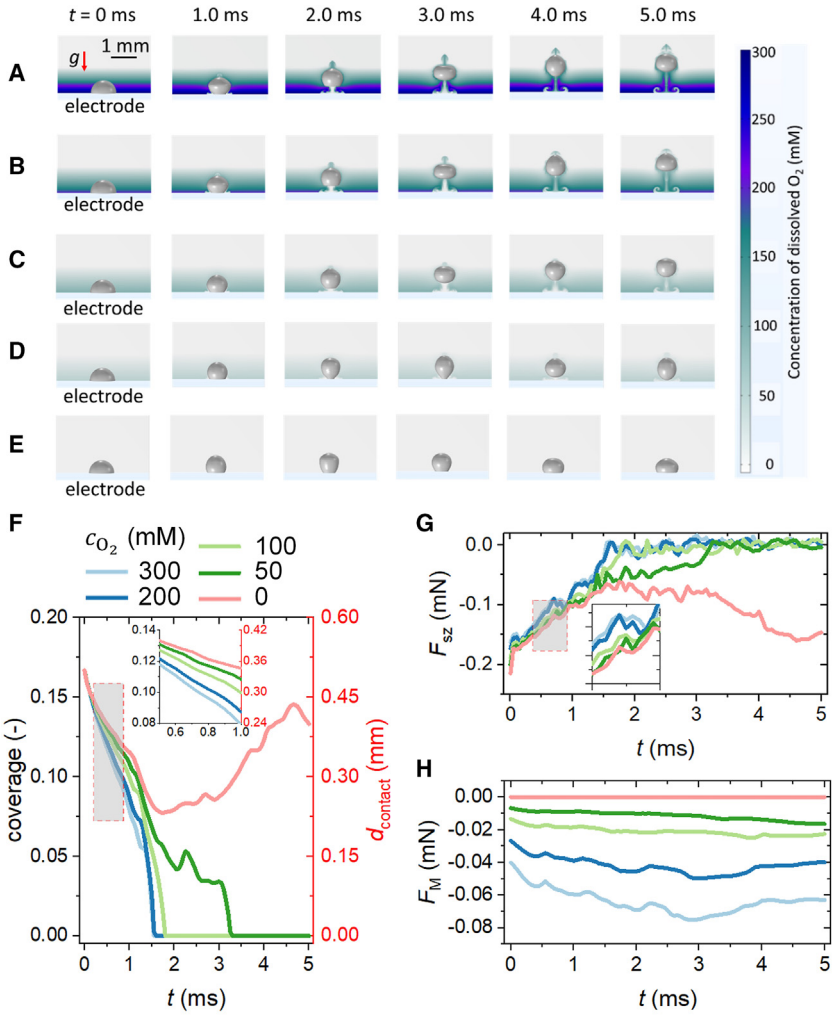

Figure 2. Effect of supersaturations on bubble detachment

(A–E) Bubble-electrolyte interface evolution color maps at various supersaturated concentrations of dissolved oxygen (c_{O_2}): (A) 300 mM (scale bar, 1 mm), (B) 200 mM, (C) 100 mM, (D) 50 mM, and (E) 0 mM.

(F) Bubble coverage on the (photo)electrode and diameter of the contact region vs. time for various c_{O_2}.

(G and H) Surface tension force component in the z direction (F_{sz}) (G) and (H) the Marangoni force, F_M, as a function of time for different c_{O_2} (H). Note that F_M is not explicitly solved during our simulation; the values are derived using Equation 1.

The insets in (F) and (G) show the magnification of the curves between 0.5 and 1 ms (as highlighted by the gray rectangle). The bubble contact angle (θ) is 60°, the thickness of the SSBL of dissolved oxygen is fixed at 1 mm, and the bubble diameter is set to 1 mm.

are negative since they are in the opposite direction of the bubble departure trajectory. Note that the contribution of F_M is already embedded inside the simulated F_{sz} as $d_{contact}$ is affected by F_M. Therefore, the bubble detachment is determined by a competition of the F_b vs. F_{sz}. The drag force, F_d, is another force that could prevent bubble departure (see Figure 1A). However, F_d is negligible when the bubble growth rate is low,[24,40] as is the case in our simulations. F_b is the main driving force for bubble detachment, and the value is constant in our simulations since bubble growth is not considered. Although F_M is not explicitly solved during our simulation, we derive the values using Equation 1, as shown in Figure 2H.

Since F_{sz} is about one order of magnitude higher than F_M, F_{sz} is the dominant force hindering bubble departure. This change in the overall force balance explains the observation of easier bubble detachment with increasing supersaturation of oxygen in the boundary layer.

The simulations above assume a linear gradient of the dissolved oxygen concentration in the SSBL. However, the gradient is more likely to be non-linear, as has been reported recently.[41] We have therefore performed additional simulations with varying concentration profiles. Although the Marangoni force (Figure S4A) is modified, F_{sz} remains nearly independent of the concentration profile function (see Figure S4B). In addition, Figure S4C shows the F_{sz} for the square root concentration profile with varying dissolved oxygen concentration; the trend is similar to that of the linear case (Figure 2G)—in other words, F_{sz} decreases with increasing concentration. More important, the impact on bubble detachment is negligible, as shown by the nearly identical profiles of bubble coverage in Figure S4D, which further confirm that F_{sz} is indeed the dominant force preventing bubble departure. Therefore, the following simulations consider the concentration of dissolved oxygen to be linearly developed in the SSBL.

Next, we evaluate the impact of different thicknesses of the SSBL of dissolved oxygen (δ_c) on the bubble detachment process. We vary δ_c from 1 to 0 mm (i.e., no SSBL), while the concentration and the bubble contact angle are kept at 300 mM and 60°, respectively. The simulation results are shown in Figure 3. A clear trend can be observed: bubbles depart easier from the electrode surface with thicker δ_c (see Figures 3A–3F), consistent with the explanation provided above. The presence of the SSBL of dissolved oxygen decreases $d_{contact}$; this effect is magnified with a thicker boundary layer, as can be seen from Figure 3G.

We briefly note that the observation that larger bubble coverage can occur for the case of δ_c = 0.2 mm vs. that for δ_c = 0 mm (see t = 0–2 ms in Figures 3E–3G) is unexpected. To understand this, we first check the corresponding F_{sz}s, as shown in Figure 3H. The magnitude of F_{sz} is higher for the case of δ_c = 0.2 mm, especially after 2 ms. We then compare the value of F_M for δ_c = 0.2 mm and δ_c = 0 mm, as shown in Figure S5. Although F_M is about one order of magnitude smaller than F_{sz}, the noticeable increase in the magnitude of F_M at ~2 ms is consistent with the bubble coverage shown in Figure 3G. The results here imply that while the presence of SSBL generally aids bubble detachment, it is only effective if the thickness of the boundary layer exceeds ~0.3 mm. When the thickness of SSBL is less than this value, the morphological change in the bubble-electrolyte interface due to variation of F_M will increase the bubble coverage and the F_{sz}, which leads to the failure of bubble detachment. It is also interesting to note the oscillatory motion of the bubble-electrolyte interface in Figures 3E–3G (also in Figures 2E and 2F), which is present because the F_b is not sufficient to overcome the F_{sz}, leading to the failure of bubble detachment. An equilibrium bubble coverage value (and contact diameter) will eventually be reached if the simulation time is extended, as shown in Figure S6. This extended simulation time is, however, beyond the scope of our present work, since our model excludes mass transfer between the bubble and electrolyte; this assumption may no longer be valid for the extended simulation time. Including O_2 mass transfer through the interface in our present model is unfortunately not trivial, and it will increase the computational cost significantly. In fact, other methods (e.g., moving mesh method)[42,43] than the level-set method are more suitable for simulating such a process, especially when the morphological change of the interface is of less interest.

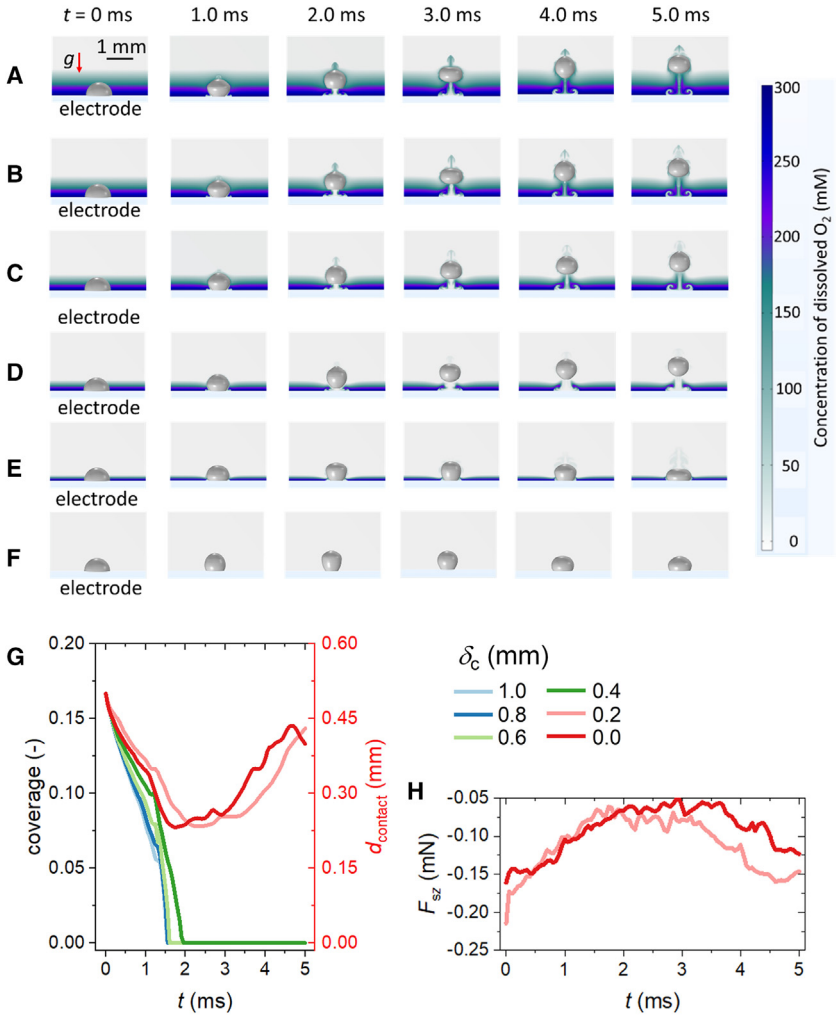

Figure 3. Effect of the thickness of the SSBL

(A–F) Bubble-electrolyte interface evolution color maps at various SSBL thicknesses of dissolved oxygen (δ_c): (A) 1.0 mm (scale bar, 1 mm), (B) 0.8 mm, (C) 0.6 mm, (D) 0.4 mm, (E) 0.2 mm, and (F) 0 mm.

(G) Bubble coverage and the diameter of the contact region as a function of time for various δ_c.

(H) Surface tension force component in the z direction (F_{sz}) for δ_c = 0.0 and 0.2 mm. The supersaturated concentration of dissolved oxygen is 300 mM, the bubble contact angle is 60°, and the bubble diameter is set to 1 mm.

The impact of contact angle (θ) is also parametrically investigated in our study, as it is known to play a crucial role in bubble departure.[44–47] Figures 4A–4C show the temporal evolution of the bubble-electrolyte interface during bubble detachment for various contact angles in the presence of the SSBL of dissolved oxygen. As the contact angle is decreased from 60° to 30°, the bubble departs the electrode surface easier. This is not surprising, since F_{sz} is proportional with sin θ, according to Equation 2. At the same time, a decreasing contact angle (i.e., increasing hydrophilicity of the electrode) leads to smaller $d_{contact}$; this can be seen clearly from the interface for different contact angles at t = 1 ms in Figure 4. The smaller contact angle further decreases the magnitude of F_{sz} and facilitates the bubble detachment process. This indicates that making the surface of the electrode hydrophilic (or aerophobic) is beneficial in terms of bubble detachment.

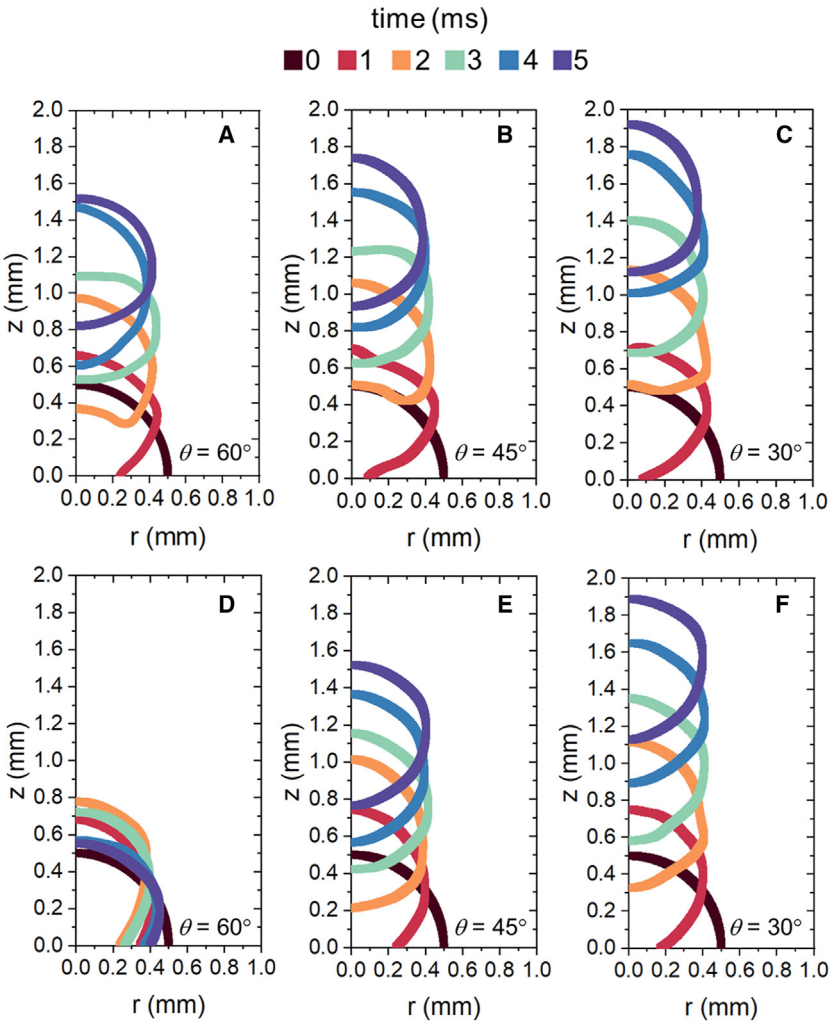

Figure 4. Effect of the contact angle

(A–C) Bubble-electrolyte interface evolution plots at different times (0–5 ms) for various bubble contact angles (θ): (A) 60°, (B) 45°, and (C) 30°, in the presence of SSBL of dissolved oxygen. c_{O_2} = 300 mM, δ_c = 1 mm, and the bubble diameter is set to 1 mm.

(D–F) The respective plots in the absence of SSBL.

The importance of the SSBL is again emphasized by comparing the detachment with and without the layer (Figures 4A–4C vs; Figures 4D–4F). Without the SSBL of dissolved oxygen, bubble detachment is hindered, especially when the bubble contact angle is large. For θ = 60°, the bubble fails to detach without the SSBL (Figure 4C), whereas it detaches easily within <2 ms in the presence of the SSBL (Figure 4A).

Implication to practical device engineering

The implication of our findings to practical device engineering can now be evaluated, as bubble adhesion on gas-evolving (photo)electrodes is an important challenge in many electrochemical systems. We first consider the relationship between forced electrolyte flow and bubble departure. Introducing a shear flow over bubbles is generally understood to induce earlier detachment and smaller departure radii.[48,49] However, in the presence of an SSBL of dissolved gas existing near the electrode, introducing a forced electrolyte flow will decrease the thickness of this

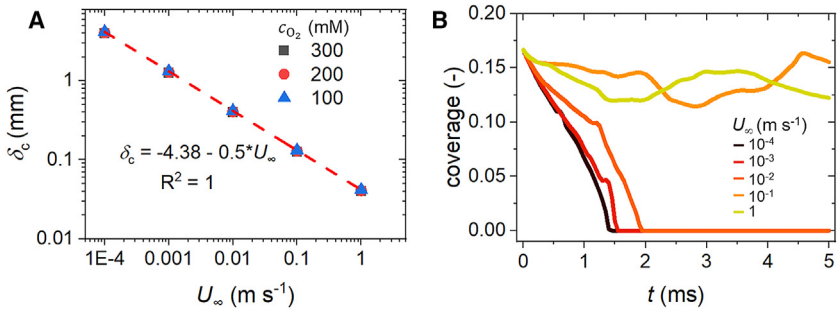

Figure 5. Effect of the electrolyte flow rate

(A) Thickness of the SSBL of dissolved oxygen at different electrolyte flow rates in the bulk, as obtained from Equation 3 and the properties shown in Figure S2.

(B) The coverage of the bubble on the (photo)electrode at different electrolyte flow rates. The bubble contact angle is set at 60°, and the diameter of the bubble is 1 mm.

SSBL. From our simulation results above (see Figure 3), this is not necessarily beneficial for bubble detachment. We therefore provide a simple model to understand how the forced electrolyte flow affects the SSBL thickness and its potential contribution to bubble detachment. Since the SSBL is analogous to the hydrodynamic boundary layer, the relationship between the thickness of the SSBL of dissolved oxygen, δ_c, and the forced electrolyte flow rate in the bulk, U_∞, can be estimated using the following equation:[50]

$$\delta_c = \frac{10}{3}\mu_{l,O_2}^{1/6} D_{O_2}^{1/3} U_\infty^{-1/2} L^{1/2} \qquad \text{(Equation 3)}$$

Here, μ_{l,O_2} is the kinematic viscosity of the electrolyte, D_{O_2} denotes the diffusion coefficient of oxygen in the electrolyte, and L is the electrode length scale. μ_{l,O_2} and D_{O_2} are considered to be concentration dependent based on previous reports in the literature (see Figure S3).[51] L is often on the order of a few centimeters, and here, we take L = 1 cm based on the size of a typical (photo)electrode in lab-scale devices. This relationship is then included in our bubble detachment model. We should note that the shear stress on the bubble-electrolyte interface due to the forced electrolyte flow is not included in our model. Therefore, our results should not be interpreted as the competition of the SSBL vs. the forced electrolyte flow on bubble detachment. Instead, our results illustrate the correlation of the forced electrolyte flow rate and the δ_c (Figure 5A) and the corresponding impact on bubble detachment (Figure 5B). As shown in Figure 5, increasing U_∞ reduces the thickness of the SSBL, which results in longer bubble adhesion on the electrode. When U_∞ is $\geq 10^{-2}$ m s^{-1}, bubble departure is completely suppressed (at least on the timescale of the simulation).

The results presented above illustrate that there are several competing factors that determine how bubble detachment from the surface of an electrode is affected by the electrolyte flow rate. At a relatively low flow rate, the presence of an SSBL likely dominates the behavior. However, as the electrolyte flow rate increases, a more pronounced shear stress, which is not included in our model, would act on the bubble-electrolyte interface. The impact on the contact angle due to this shear stress will become more dominant than the effect of the SSBL.[8] Thus, higher electrolyte flow rate would facilitate bubble detachment, although it comes with an energetic penalty as higher pumping power is required to maintain such a high flow rate. The impact of the electrolyte flow rate on product separation should, of course, also be considered.[2] Altogether, an optimum electrolyte flow rate likely exists for the

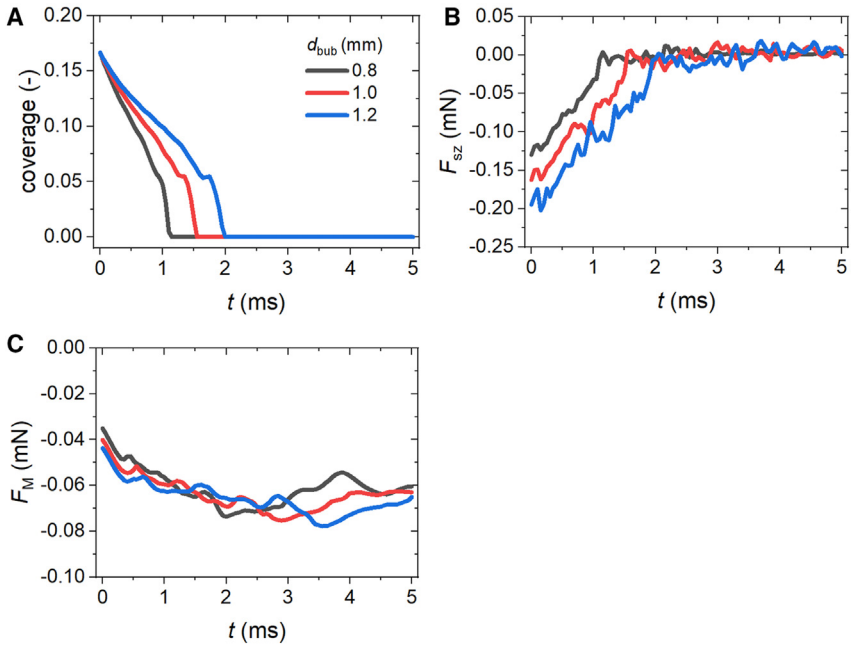

Figure 6. Effect of bubble size

(A–C) (A) Bubble coverage, (B) the surface tension force in the z direction (F_{sz}), and (C) the Marangoni force (F_M). The contact angle of the bubble-electrolyte interface and the (photo) electrode surface is set to 60°, the concentration of the SSBL is 300 mM, the thickness of the SSBL is 1 mm.

operation of the (photo)electrochemical reactors at which bubbles can depart easily from the gas-evolving (photo)electrode with the assistance of the SSBL of dissolved product and the shear stress on the bubble-electrolyte interface, with acceptable pumping power and sufficient product separation. This is especially crucial when considering large-scale (photo)electrochemical reactors operating for long periods of time.

Insights from our simulation results also allow us to discuss the possible effect of increased operating pressure on bubble detachment. Most commercial electrolyzers operate at high pressure,[52–54] motivated by the possibility of avoiding (or reducing) compression cost or of allowing direct utilization of the products in high-pressure downstream processes (e.g., chemical synthesis with H_2). It has recently been suggested that operating photoelectrochemical reactors at higher pressure would be attractive,[55] since this would mitigate some of the adverse effects of bubble formation. At higher pressure, Henry's law dictates that the solubility of gaseous products will increase. This will increase the concentration of dissolved gas in the SSBL and its thickness, and it would thus facilitate bubble detachment from the surface of the (photo)electrode (see Figure 2 and the prior discussion). However, a higher pressure decreases the size of the bubbles.[25,56] The F_b of these smaller bubbles is proportional to the cube of the bubble diameter and may not be sufficient to initiate detachment (i.e., the bubbles will continue to adhere to the electrode). The overall impact of increased pressure operation on bubble detachment is therefore not obvious and warrants special attention.

Using our multiphysics model, we can emulate the effect of increasing pressure by adjusting the bubble size to smaller values. Figure 6A shows the bubble coverage

as a function of time for these differently sized bubbles. The bubble with a diameter of 0.8 mm detaches faster from the electrode than those with larger diameters (e.g., 1.0 and 1.2 mm). This trend contradicts that of the F_b. It, however, agrees with the trend of the F_{sz}, which points toward the electrode surface and is proportional to the bubble coverage area. Figure 6B compares F_{sz} of these differently sized bubbles. Note that the contact angle is fixed as 60°—in other words, the hydrophilicity of the (photo)electrode is assumed to be independent of the change in hydrostatic pressure. The assumption is reasonable, as supported by a recent experimental study of a water-N_2-polytetrafluoroethylene system.[57] In that study, the contact angle of the water droplet was measured under various pressures and temperatures, and pressure elevation up to 50 bar introduced only minor changes to the contact angle. The magnitude of F_{sz} increases with increasing bubble diameter, which explains how smaller bubbles are preferred for easier detachment. Again, this observation indicates that surface tension is the determining factor affecting bubble detachment from an electrode, not the F_b. Note that the Marangoni force F_M was also investigated for the different bubble sizes, as shown in Figure 6C. There appears to be a minor dependence on bubble size, especially at t close to zero, but since F_M is about one order of magnitude smaller than F_{sz}, its impact is negligible. Overall, it can be concluded that although the bubble diameter decreases with increasing pressure, thereby decreasing the F_b, small-sized bubbles depart from the electrode faster due to the smaller F_{sz} induced by the SSBL of dissolved gas and the smaller coverage area. This represents a potential benefit of operating (photo)electrochemical cells at higher pressure.

Finally, we note that our model focused on the effect of supersaturation of the dissolved gas on bubble detachment from planar (photo)electrodes, with the main mechanism being a solutal Marangoni force that emerged due to the surface tension gradient. The supersaturation of O_2 is taken as a variable in our simulations. In practice, the supersaturation of gases during water electrolysis will be altered by various parameters, such as hydrostatic pressure, temperature, forced electrolyte flow rate, current density, and electrolytes. In our work, we showed how the gas supersaturation can be affected by the forced electrolyte flow rate in the bulk and the corresponding effect on bubble detachment. These operating parameters can be practically engineered in devices to facilitate bubble detachment. Another practical implication of our study is in the effect of surface tension gradient to the Marangoni effect and bubble detachment. Other than gas supersaturation, the surface tension gradient may also be affected by the presence of, for example, the temperature gradient during (photo)electrolysis (see the schematic in Figure 1A). This thermal effect is ignored in our work, due to relatively low current density (10–20 mA cm^{-2}) under standard solar irradiation. However, when (photo)electrochemical water splitting is conducted under concentrated sunlight, the current density may reach the same order of magnitude as that in commercial water electrolyzers (i.e., 0.5–2 A cm^{-2}).[58,59] A "desirable" temperature gradient (i.e., facilitating bubble detachment) could therefore be obtained by careful cell engineering.

In summary, we have developed a multiphysics model to elucidate the role of the SSBL of dissolved oxygen on the bubble detachment from the surface of a (photo) electrode. The model combines the Navier-Stokes equation and the level-set method to resolve the liquid flow velocity and capture the motion of the bubble-electrolyte interface. Convection of dissolved oxygen was also considered in the model. Simulations using our model reveal that the SSBL plays a critical role in bubble detachment. Noticeable changes in the shape of the bubbles at the bubble-electrolyte interface could be observed in the presence of the SSBL, driven by the

concentration-dependent Marangoni effect. Specifically, the concentration gradient in the SSBL induces a gradient in surface tension (i.e., shear stress acting on the bubble-electrolyte interface). This morphological change significantly affects the F_{sz} component in the z direction, F_{sz}, which is the dominant force preventing bubble departure from the surface of the (photo)electrode. Our simulation results show that F_{sz} decreases with increasing concentration of oxygen, increasing the thickness of the SSBL and decreasing the bubble contact angle. Based on these findings, we propose several practical engineering considerations for (photo)electrochemical devices. We show that competing factors between the presence of the SSBL, shear stress due to the forced electrolyte flow, and pumping power need to be considered carefully as they would determine how bubble detachment from a (photo)electrode is impacted by the electrolyte flow rate. Finally, supersaturation of the boundary layer with dissolved oxygen is shown to significantly facilitate the detachment of bubbles with smaller sizes due to smaller F_{sz}. This represents a potential benefit of operating photoelectrochemical reactors at elevated pressure.

EXPERIMENTAL PROCEDURES

Resource availability

Lead contact

Further information and requests for resources and reagents should be directed to and will be fulfilled by the lead contact, Fatwa F. Abdi (ffabdi@cityu.edu.hk).

Materials availability

This study did not generate new unique materials.

Data and code availability

All data reported in this paper are included in Data S1, as well as in the main text and the supplemental information. The multiphysics model files used in this study are available from the lead contact upon reasonable request. Any additional information required to reanalyze the data reported in this paper is available from the lead contact upon reasonable request.

Fluid dynamics

To model the physics encountered during a two-phase flow with a moving boundary, (a gas bubble detaching from an electrode in our case), the momentum equations need to be solved for the fluids as well as the motion of the interface. The following continuity equation for incompressible Newtonian fluids that conserves mass was considered:

$$\nabla \cdot \vec{u} = 0 \qquad \text{(Equation 4)}$$

where $\vec{u}$ is the velocity field. Furthermore, because the flow is incompressible, the density of the fluid phase (ρ) is constant. This means that the only way to change the mass of the computational domain (Ω) is by convection, which is expressed in the following equation.

$$\rho\left(\frac{\partial \vec{u}}{\partial t} + (\vec{u}\cdot\nabla)\vec{u}\right) = -\nabla p + \nabla\cdot\left(\mu\left(\nabla\vec{u} + (\nabla\vec{u})^{T}\right)\right) + \rho g\vec{e}_{g} + \vec{F}_{sa} \qquad \text{(Equation 5)}$$

Momentum conservation was solved using this Navier-Stokes equation with a surface tension term. p is the pressure, $\vec{F}_{sa}$ is the surface tension force, and μ is the dynamic viscosity. The surface tension force is modeled with the continuum surface force model.[60] The left-hand side of Equation 5 contains a time-dependent term and a convection term, while the right-hand side contains a pressure term, a viscous dissipation term, a gravity term, and a surface tension force term.

Level-set method

The motion of the bubble-electrolyte interface was simulated using the level-set method, which is a technique to represent moving interfaces or boundaries using a fixed mesh.[35,49,61] The interface was represented by a certain level set or isocontour of a globally defined function, the level-set function, ϕ. ϕ is a smoothed signed distance function, and its values range from 0 to 1. In our case, $\phi = 0$ is the domain of the gas bubble, while $\phi = 1$ represents the liquid phase domain. The interface is therefore denoted by $\phi = 0.5$. Both phases have significantly different densities and viscosities, which causes a large discontinuity across the interface. To improve the numerical robustness, a smeared Heaviside function is used.

$$H(\phi) = \begin{cases} 0 \text{ for } \phi < -\epsilon \\ \frac{1}{2} + \frac{\phi}{2} + \frac{1}{2\pi}\sin\left(\frac{\pi\phi}{\epsilon}\right) \quad \text{for } -\epsilon < \phi < \epsilon \\ 1 \text{ for } \phi > \epsilon \end{cases} \qquad \text{(Equation 6)}$$

The parameter ϵ determines the thickness of the region where ϕ goes smoothly from 0 to 1 and is typically of the same order as the mesh element size. By default, ϵ is constant and equals half of the largest mesh size, h_{max}, within the domain.

The modeling interface solves the following equation to move the interface with the velocity field $\vec{u}$:

$$\frac{\partial\phi}{\partial t} + \vec{u}\cdot\nabla\phi = \gamma\nabla\cdot\left(\epsilon\nabla\phi - \phi(1-\phi)\frac{\nabla\phi}{|\nabla\phi|}\right) \qquad \text{(Equation 7)}$$

The terms on the left-hand side describe the (constrained) motion of the interface, while those on the right-hand side are necessary for numerical stability. The parameter γ determines the amount of reinitialization or stabilization of the level set function, which was individually tuned for each specific problem. A suitable value for γ is the maximum magnitude of the velocity field $\vec{u}$.

Similarly, the density and viscosity can be written as a function of the level-set function.

$$\rho = \rho_1 + (\rho_2 - \rho_1)\phi \qquad \text{(Equation 8)}$$

$$\mu = \mu_1 + (\mu_2 - \mu_1)\phi \qquad \text{(Equation 9)}$$

where index 1 represents the part of the domain in which the level-set function is smaller than 0.5, and index 2 denotes the region where its value is greater than 0.5.

Transport of dissolved product

The mass transport of the dissolved gas product was solved based on the theory of diluted species,

$$\frac{dc_i}{dt} = -\nabla\cdot N_i = -\nabla\cdot(c_i\vec{u}) \qquad \text{(Equation 10)}$$

where c_i is the concentration of the dissolved product, N_i is the molar flux of the dissolved gas, and $\vec{u}$ represents the liquid velocity, which was obtained by solving Equation 5. An example of the liquid flow velocity can be found in Figure S7. Note that only the convective mass transfer of the dissolved product was considered, and the diffusion process was excluded. This assumption could be justified because diffusion is relatively slow (compared to the convective flow rates studied here) and is unlikely to make a considerable contribution within the simulation time in this study (5 ms).

Numerical treatment

The multiphysics model was solved in a fully coupled mode, using the built-in PARDISO solver in COMSOL Multiphysics 5.6. The pressure velocity coupling was discretized by a P1 + P1 scheme, and the level set variable was discretized with linear elements. As a time-stepping algorithm, the generalized alpha method was used with an automatic time-step choice. The time resolution of the results dataset was 0.05 ms. The simulations were performed on a high-performance work station (Intel Xeon CPU E5-2650 v2, 32 physical cores, 192 GB RAM). A relative tolerance of 0.005 was set as the convergence criterion. The variables and parameters used in our simulations are tabulated in Tables S1–S3.

Model and mesh independence validation

Our numerical model was validated against the volume-of-fluid-based model developed by Vachaparambil et al.[50] This model has been validated by comparing against several experimental and numerical studies (see Figures 3 and 6 of Vachaparambil et al.[50]). The comparison between our model and the model used by Vachaparambil et al. is shown in Figure S8. The predicted evolution of the bubble-electrolyte interface from our model agrees very well with the results shown by Vachaparambil et al.

The mesh independence of the present model was evaluated by solving the bubble-electrolyte interface at 5 ms with different mesh resolutions (i.e., maximum element size). As indicated in Figure S9A, the difference between the bubble-electrolyte interface solved using 0.014 mm vs. 0.012 mm is marginal. However, the computation time for the more refined mesh resolution more than doubled (see Figure S9B). Therefore, 0.014 mm was chosen as the mesh resolution in our simulations. The optimized mesh for our simulation is shown in Figure S10. Note that the boundary between the two phases was used for phase initialization. After the simulation started, the bubble-electrolyte interface evolved spatially as simulated using the level-set method. Therefore, a refined mesh was needed for the overall domain, instead of only refining the mesh at, for example, the contact angle region. As a reference, the overall number of meshes is 143,187, with an average mesh quality of 0.96.

SUPPLEMENTAL INFORMATION

Supplemental information can be found online at https://doi.org/10.1016/j.xcrp.2024.102069.

ACKNOWLEDGMENTS

We gratefully acknowledge the Helmholtz Association of German Research Centers and the Federal Ministry of Education and Research, Germany for supporting the development of solar-powered technologies for H_2 generation within the framework of the Innovation Pool project "Solar H_2: Highly Pure and Compressed" and the Helmholtz Research Program "Materials and Technologies for the Energy Transition." Part of the work was also carried out with the support of the Helmholtz Energy Materials Foundry, a large-scale distributed research infrastructure founded by the German Helmholtz Association (GZ 714-48172-21/1). We also thank Prof. Pavlina Basarova and Jakub Crha at the University of Chemistry and Technology, Prague, as well as Dr. Annette Pahl at COMSOL for the valuable suggestions made during the development of our model.

AUTHOR CONTRIBUTIONS

Conceptualization, F.L. and F.F.A. Methodology, F.L. and F.F.A. Investigation, F.L. Writing – original draft, F.L. Writing – review & editing, F.L., R.v.d.K., and F.F.A. Supervision, R.v.d.K. and F.F.A. Funding acquisition, R.v.d.K. and F.F.A.

DECLARATION OF INTERESTS

The authors declare no competing interests.

Received: February 3, 2024
Revised: May 4, 2024
Accepted: June 6, 2024
Published: June 28, 2024

REFERENCES

1. Vogt, H. (2017). The quantities affecting the bubble coverage of gas-evolving electrodes. Electrochim. Acta *235*, 495–499. https://doi.org/10.1016/j.electacta.2017.03.116.

2. Obata, K., Mokeddem, A., and Abdi, F.F. (2021). Multiphase fluid dynamics simulations of product crossover in solar-driven, membrane-less water splitting. Cell Rep. Phys. Sci. *2*, 100358. https://doi.org/10.1016/j.xcrp.2021.100358.

3. Mazloomi, K., Sulaiman, N.B., and Moayedi, H. (2012). Electrical efficiency of electrolytic hydrogen production. Int. J. Electrochem. Sci. *7*, 3314–3326. https://doi.org/10.1016/S1452-3981(23)13957-5.

4. Wang, C.-C., and Chen, C.-Y. (2009). Water electrolysis in the presence of an ultrasonic field. Electrochim. Acta *54*, 3877–3883. https://doi.org/10.1016/j.electacta.2009.01.087.

5. Al-Fetlawi, H., Shah, A., and Walsh, F. (2010). Modelling the effects of oxygen evolution in the all-vanadium redox flow battery. Electrochim. Acta *55*, 3192–3205. https://doi.org/10.1016/j.electacta.2009.12.08.

6. Weber, A.Z., Mench, M.M., Meyers, J.P., Ross, P.N., Gostick, J.T., and Liu, Q. (2011). Redox flow batteries: a review. J. Appl. Electrochem. *41*, 1137–1164. https://doi.org/10.1007/s10800-011-0348-2.

7. Holmes-Gentle, I., Bedoya-Lora, F., Alhersh, F., and Hellgardt, K. (2018). Optical losses at gas evolving photoelectrodes: implications for photoelectrochemical water splitting. J. Phys. Chem. C *123*, 17–28. https://doi.org/10.1021/acs.jpcc.8b07732.

8. Groß, T., Bauer, J., Ludwig, G., Fernandez Rivas, D., and Pelz, P. (2018). Bubble nucleation from micro-crevices in a shear flow: Experimental determination of nucleation rates and surface nuclei growth. Exp. Fluid *59*, 1–10. https://doi.org/10.1007/s00348-017-2459-y.

9. Eigeldinger, J., and Vogt, H. (2000). The bubble coverage of gas-evolving electrodes in a flowing electrolyte. Electrochim. Acta *45*, 4449–4456. https://doi.org/10.1016/S0013-4686(00)00513-2.

10. Liu, B., Wu, C., Chen, G., Chen, W., Peng, L., Yao, Y., Wei, Z., Zhu, H., Han, T., and Tang, D. (2019). All-in-one surface engineering strategy on nickel phosphide arrays towards a robust electrocatalyst for hydrogen evolution reaction. J. Power Sources *429*, 46–54. https://doi.org/10.1016/j.jpowsour.2019.04.119.

11. Liu, Y., and Dillon, S.J. (2014). In situ observation of electrolytic H 2 evolution adjacent to gold cathodes. Chem. Commun. *50*, 1761–1763. https://doi.org/10.1039/C3CC46737F.

12. Sabahi, N., Razfar, M.R., and Hajian, M. (2017). Experimental investigation of surfactant-mixed electrolyte into electrochemical discharge machining (ECDM) process. J. Mater. Process. Technol. *250*, 190–202. https://doi.org/10.1016/j.jmatprotec.2017.07.017.

13. Zhao, X., Ren, H., and Luo, L. (2019). Gas bubbles in electrochemical gas evolution reactions. Langmuir *35*, 5392–5408. https://doi.org/10.1021/acs.langmuir.9b00119.

14. Xu, Y., Chen, J., Jiang, B., Liu, Y., and Ni, J. (2018). Experimental investigation of magnetohydrodynamic effect in electrochemical discharge machining. Int. J. Mech. Sci. *142–143*, 86–96. https://doi.org/10.1016/j.ijmecsci.2018.04.020.

15. Fernández, D., Martine, M., Meagher, A., Möbius, M.E., and Coey, J. (2012). Stabilizing effect of a magnetic field on a gas bubble produced at a microelectrode. Electrochem. Commun. *18*, 28–32. https://doi.org/10.1016/j.elecom.2012.01.016.

16. Offin, D.G., Birkin, P.R., and Leighton, T.G. (2014). An electrochemical and high-speed imaging study of micropore decontamination by acoustic bubble entrapment. Phys. Chem. Chem. Phys. *16*, 4982–4989. https://doi.org/10.1039/C3CP55088E.

17. Birkin, P.R., Offin, D.G., Vian, C.J.B., and Leighton, T.G. (2015). Electrochemical 'bubble swarm'enhancement of ultrasonic surface cleaning. Phys. Chem. Chem. Phys. *17*, 21709–21715. https://doi.org/10.1039/C5CP02933C.

18. Sakuma, G., Fukunaka, Y., and Matsushima, H. (2014). Nucleation and growth of electrolytic gas bubbles under microgravity. Int. J. Hydrogen Energy *39*, 7638–7645. https://doi.org/10.1016/j.ijhydene.2014.03.059.

19. Tawfik, M., and Diez, F. (2014). On the relation between onset of bubble nucleation and gas supersaturation concentration. Electrochim. Acta *146*, 792–797. https://doi.org/10.1016/j.electacta.2014.08.147.

20. Matsushima, H., Kiuchi, D., Fukunaka, Y., and Kuribayashi, K. (2009). Single bubble growth during water electrolysis under microgravity. Electrochem. Commun. *11*, 1721–1723. https://doi.org/10.1016/j.elecom.2009.07.009.

21. Yang, X., Karnbach, F., Uhlemann, M., Odenbach, S., and Eckert, K. (2015). Dynamics of single hydrogen bubbles at a platinum microelectrode. Langmuir *31*, 8184–8193. https://doi.org/10.1021/acs.langmuir.5b01825.

22. Jaikumar, A., and Kandlikar, S.G. (2016). Pool boiling enhancement through bubble induced convective liquid flow in feeder microchannels. Appl. Phys. Lett. *108*, 041604. https://doi.org/10.1063/1.4941032.

23. Vogt, H., and Balzer, R. (2005). The bubble coverage of gas-evolving electrodes in stagnant electrolytes. Electrochim. Acta *50*, 2073–2079. https://doi.org/10.1016/j.electacta.2004.09.025.

24. Chen, J., Guo, L., Hu, X., Cao, Z., and Wang, Y. (2018). Dynamics of single bubble departure from TiO2 nanorod-array photoelectrode. Electrochim. Acta *274*, 57–66. https://doi.org/10.1016/j.electacta.2018.04.051.

25. Iwata, R., Zhang, L., Wilke, K.L., Gong, S., He, M., Gallant, B.M., and Wang, E.N. (2021). Bubble growth and departure modes on wettable/non-wettable porous foams in alkaline water splitting. Joule *5*, 887–900. https://doi.org/10.1016/j.joule.2021.02.015.

26. Bashkatov, A., Hossain, S.S., Yang, X., Mutschke, G., and Eckert, K. (2019). Oscillating hydrogen bubbles at pt microelectrodes. Phys. Rev. Lett. *123*, 214503. https://doi.org/10.1103/PhysRevLett.123.214503.

27. Lubetkin, S. (2002). The motion of electrolytic gas bubbles near electrodes. Electrochim. Acta *48*, 357–375. https://doi.org/10.1016/S0013-4686(02)00682-5.

28. Yang, X., Baczyzmalski, D., Cierpka, C., Mutschke, G., and Eckert, K. (2018). Marangoni convection at electrogenerated hydrogen bubbles. Phys. Chem. Chem. Phys. *20*, 11542–11548. https://doi.org/10.1039/C8CP01050A.

29. Massing, J., Mutschke, G., Baczyzmalski, D., Hossain, S.S., Yang, X., Eckert, K., and Cierpka, C. (2019). Thermocapillary convection during hydrogen evolution at microelectrodes. Electrochim. Acta *297*, 929–940. https://doi.org/10.1016/j.electacta.2018.11.187.

30. Meulenbroek, A., Vreman, A., and Deen, N. (2021). Competing Marangoni effects form a stagnant cap on the interface of a hydrogen bubble attached to a microelectrode. Electrochim. Acta *385*, 138298. https://doi.org/10.1016/j.electacta.2021.138298.

31. Park, S., Liu, L., Demirkır, Ç., van der Heijden, O., Lohse, D., Krug, D., and Koper, M.T.M. (2023). Solutal Marangoni effect determines bubble dynamics during electrocatalytic hydrogen evolution. Nat. Chem. *15*, 1532–1540. https://doi.org/10.1038/s41557-023-01294-y.

32. Hossain, S.S., Mutschke, G., Bashkatov, A., and Eckert, K. (2020). The thermocapillary effect on

gas bubbles growing on electrodes of different sizes. Electrochim. Acta *353*, 136461. https://doi.org/10.1016/j.electacta.2020.136461.

33. Vogt, H. (1984). The rate of gas evolution at electrodes—II. An estimate of the efficiency of gas evolution on the basis of bubble growth data. Electrochim. Acta *29*, 175–180. https://doi.org/10.1016/0013-4686(84)87044-9.

34. Zahedi, S., Kronbichler, M., and Kreiss, G. (2012). Spurious currents in finite element based level set methods for two-phase flow. Int. J. Numer. Methods Fluids *69*, 1433–1456. https://doi.org/10.1002/fld.2643.

35. Crha, J., Basařová, P., Ruzicka, M.C., Kašpar, O., and Zednikova, M. (2021). Comparison of Two Solvers for Simulation of Single Bubble Rising Dynamics: COMSOL vs. Fluent. Minerals *11*, 452. https://doi.org/10.3390/min11050452.

36. Afkhami, S., Zaleski, S., and Bussmann, M. (2009). A mesh-dependent model for applying dynamic contact angles to VOF simulations. J. Comput. Phys. *228*, 5370–5389. https://doi.org/10.1016/j.jcp.2009.04.027.

37. Bowers, P.G., Hofstetter, C., Letter, C.R., and Toomey, R.T. (1995). Supersaturation limit for homogeneous nucleation of oxygen bubbles in water at elevated pressure:" Super-Henry's Law". J. Phys. Chem. *99*, 9632–9637. https://doi.org/10.1021/j100023a048.

38. Hossain, S.S., Bashkatov, A., Yang, X., Mutschke, G., and Eckert, K. (2022). Force balance of hydrogen bubbles growing and oscillating on a microelectrode. Phys. Rev. E *106*, 035105. https://doi.org/10.1103/PhysRevE.106.035105.

39. Zhan, S., Yuan, R., Wang, X., Zhang, W., Yu, K., Li, B., Wang, Z., and Wang, J. (2023). Dynamics of growth and detachment of single hydrogen bubble on horizontal and vertical microelectrode surfaces considering liquid microlayer structure in water electrolysis. Phys. Fluids *35*, 032111. https://doi.org/10.1063/5.0141648.

40. Cao, Z., Feng, Y., Zhang, B., Xu, Q., Wang, Y., and Guo, L. (2022). Regulation of bubble behavior on a TiO2 photoelectrode surface during photoelectrocatalytic water splitting. J. Phys. Chem. C *126*, 12480–12491. https://doi.org/10.1021/acs.jpcc.2c03100.

41. Zhao, P., Zhang, C., and Gong, S. (2023). Size Ranges of Effective Nucleation Cavities on Gas-Evolving Surfaces. Langmuir *39*, 16101–16110. https://doi.org/10.1021/acs.langmuir.3c02235.

42. Gutiérrez, E., Balcázar, N., Bartrons, E., and Rigola, J. (2017). Numerical study of Taylor bubbles rising in a stagnant liquid using a level-set/moving-mesh method. Chem. Eng. Sci. *164*, 158–177. https://doi.org/10.1016/j.ces.2017.02.018.

43. Tuković, Ž., and Jasak, H. (2012). A moving mesh finite volume interface tracking method for surface tension dominated interfacial fluid flow. Computers & Fluids *55*, 70–84. https://doi.org/10.1016/j.compfluid.2011.11.003.

44. Bae, M., Kang, Y., Lee, D.W., Jeon, D., and Ryu, J. (2022). Superaerophobic polyethyleneimine hydrogels for improving electrochemical hydrogen production by promoting bubble detachment. Adv. Energy Mater. *12*, 2201452. https://doi.org/10.1002/aenm.202201452.

45. Brussieux, C., Viers, P., Roustan, H., and Rakib, M. (2011). Controlled electrochemical gas bubble release from electrodes entirely and partially covered with hydrophobic materials. Electrochim. Acta *56*, 7194–7201. https://doi.org/10.1016/j.electacta.2011.04.104.

46. Kim, B.K., Kim, M.J., and Kim, J.J. (2021). Impact of surface hydrophilicity on electrochemical water splitting. ACS Appl. Mater. Interfaces *13*, 11940–11947. https://doi.org/10.1021/acsami.0c22409.

47. Angulo, A., van der Linde, P., Gardeniers, H., Modestino, M., and Fernández Rivas, D. (2020). Influence of bubbles on the energy conversion efficiency of electrochemical reactors. Joule *4*, 555–579. https://doi.org/10.1016/j.joule.2020.01.005.

48. Duhar, G., and Colin, C. (2006). Dynamics of bubble growth and detachment in a viscous shear flow. Phys. Fluids *18*, 077101. https://doi.org/10.1063/1.2213638.

49. Oguz, H.N., and Prosperetti, A. (1993). Dynamics of bubble growth and detachment from a needle. J. Fluid Mech. *257*, 111–145. https://doi.org/10.1017/S0022112093003015.

50. Vachaparambil, K.J., and Einarsrud, K.E. (2021). Numerical simulation of continuum scale electrochemical hydrogen bubble evolution. Appl. Math. Model. *98*, 343–377. https://doi.org/10.1016/j.apm.2021.05.007.

51. Atkins, P., De Paula, J., and Keeler, J. (2023). Atkins' Physical Chemistry (Oxford University Press).

52. Ramdin, M., Morrison, A.R.T., De Groen, M., Van Haperen, R., De Kler, R., van den Broeke, L.J.P., Trusler, J.P.M., De Jong, W., and Vlugt, T.J.H. (2019). High pressure electrochemical reduction of CO2 to formic acid/formate: a comparison between bipolar membranes and cation exchange membranes. Ind. Eng. Chem. Res. *58*, 1834–1847. https://doi.org/10.1021/acs.iecr.8b04944.

53. Afshari, E., Khodabakhsh, S., Jahantigh, N., and Toghyani, S. (2021). Performance assessment of gas crossover phenomenon and water transport mechanism in high pressure PEM electrolyzer. Int. J. Hydrogen Energy *46*, 11029–11040. https://doi.org/10.1016/j.ijhydene.2020.10.180.

54. Espinosa-López, M., Darras, C., Poggi, P., Glises, R., Baucour, P., Rakotondrainibe, A., Besse, S., and Serre-Combe, P. (2018). Modelling and experimental validation of a 46 kW PEM high pressure water electrolyzer. Renew. Energy *119*, 160–173. https://doi.org/10.1016/j.renene.2017.11.081.

55. Ivanova, M.E., Peters, R., Müller, M., Haas, S., Seidler, M.F., Mutschke, G., Eckert, K., Röse, P., Calnan, S., Bagacki, R., et al. (2023). Technological Pathways to Produce Compressed and Highly Pure Hydrogen from Solar Power. Angew. Chem. Int. Ed. Engl. *62*, e202218850. https://doi.org/10.1002/anie.202218850.

56. Janssen, L., Sillen, C., Barendrecht, E., and Van Stralen, S. (1984). Bubble behaviour during oxygen and hydrogen evolution at transparent electrodes in KOH solution. Electrochim. Acta *29*, 633–642. https://doi.org/10.1016/0013-4686(84)87122-4.

57. Song, J.-W., Ma, M.-C., and Fan, L.-W. (2020). Understanding the temperature dependence of contact angles of water on a smooth hydrophobic surface under pressurized conditions: An experimental study. Langmuir *36*, 9586–9595. https://doi.org/10.1021/acs.langmuir.0c01671.

58. Tembhurne, S., Nandjou, F., and Haussener, S. (2019). A thermally synergistic photo-electrochemical hydrogen generator operating under concentrated solar irradiation. Nat. Energy *4*, 399–407. https://doi.org/10.1038/s41560-019-0373-7.

59. Holmes-Gentle, I., Bedoya-Lora, F.E., Aimone, L., and Haussener, S. (2023). Photoelectrochemical behaviour of photoanodes under high photon fluxes. J. Mater. Chem. A Mater. *11*, 23895–23908. https://doi.org/10.1039/D3TA05257E.

60. Brackbill, J.U., Kothe, D.B., and Zemach, C. (1992). A continuum method for modeling surface tension. J. Comput. Phys. *100*, 335–354. https://doi.org/10.1016/0021-9991(92)90240-Y.

61. Osher, S., Fedkiw, R., and Piechor, K. (2004). Level set methods and dynamic implicit surfaces. Appl. Mech. Rev. *57*, B15. https://doi.org/10.1115/1.1760521.